POLarimetry with Cadmium telluride Array (POLCA) IV

Evaluation of scattering polarimetric capabilities of a two layer CdTe Array prototype for hard X- and gamma-ray astronomy

Experiment No MI-1275 Report

Proposer:
Ezio CAROLI, INAF/IASF-Bologna, Via Gobetti 101, Bologna, Italy

Co-proposers:
Natalia AURICCHIO, INAF/IASF-Bologna, Italy
Rui Miguel CURADO DA SILVA, LIP-Coimbra and Universidade de Coimbra, Portugal
Stefano DEL SORDO, INAF/IASF-Palermo, Italy
Jorge Manuel MAIA PEREIRA, Universidade da Beira Interior, Covilhã, Portugal
Miguel MOITA, Universidade de Coimbra, Portugal
John Buchan STEPHEN, INAF/IASF-Bologna, Italy

Participants to beam tests:
Ezio Caroli, INAF/IASF-Bologna, Italy
John Buchan Stephen, INAF/IASF-Bologna, Italy
Natalia Auricchio, INAF/IASF-Bologna, Italy
Jorge Manuel MAIA PEREIRA, Universidade da Beira Interior, Covilhã, Portugal
Miguel MOITA, Universidade de Coimbra, Portugal
Marcela Pascoa, Universidade de Coimbra, Portugal

Beamline:	**ID 15A**
Responsible:	Dr. Marco di Michiel
Local contact(s):	Thomas BUSLAPS
Shift Period:	27 September 2017 (at 16:00) - 1 October 2017 (at 16:00)
Number of shift:	12

Table of Contents

TABLE OF CONTENTS **2**

1 SUMMARY **3**

2 INTRODUCTION **4**

3 COMPTON SCATTERING POLARIMETRY **5**

4 COMPTON-POLCA IV SYSTEM MAIN CHARACTERISTICS **7**

4.1 DETECTION SYSTEM 8
4.2 READ OUT ELECTRONICS TAKES 9
4.3 ACQUISITION SOFTWARE 9

5 EXPERIMENT PREPARATION AT LIP-COIMBRA **10**

5.1 ASIC OPERATIVE SETTING 10
5.2 DETECTOR STATUS BEFORE THE ESRF TEST CAMPAIGN 10
5.3 MULTIPARAMETRIC ELECTRONICS CHAIN EQUALIZATION 11
5.4 DETECTOR SYSTEM CALIBRATION 12

6 ESRF ID15 A BEAMLINE **13**

7 ESRF DATA ANALYSIS **15**

7.1 PIXEL RESPONSE UNIFORMITY 15
7.1.1 Detectors evaluation *15*
7.1.2 Spectroscopic performance *16*
7.1.3 Event efficiency *17*
7.2 POLARIMETRIC PERFORMANCE EVALUATION 17
7.2.1 Data Selection and Corrections *17*
7.2.2 Intra layer polarimetric performance *19*
7.2.3 Dual layer polarimetric performance *20*

8 CONCLUSIONS AND FURTHER WORK **23**

REFERENCES **25**

1 Summary

Polarimetry has been increasingly recognized as an important observational parameter for high energy astrophysics. However, polarimetry in high-energy astrophysics has been insufficiently explored due to the complexity of the required detector systems: detection, electronic and signal processing systems. Herein we study a new prototype in two layers Compton configuration based on two CdTe spectro-imagers operated in coincidence within 100 keV up to 600 keV energy range. The two CdTe detectors have an anode segmented in 8 x 8 pixels (2 mm pitch) on 2 mm thick crystals. The new detection system configuration allows to assess the scattering polarimetric performance of a 3D spectro-imager by changing the distance between the two CdTe pixel detection layers. The prototype measured performances provide useful data to optimize a spectro-imager with polarimetric capabilities for both high efficiency Laue lens telescope focal plane and all sky advanced Compton telescope design for next generation space missions.

This document reports on the experiment MI-1275 done at the beamline ID15A in the European Synchrotron Radiation Facility (ESRF) between 26 September and 2 October of 2017. The device available at ID15A was the U22 undulator, which delivers sufficient flux energies up to $300\ \mathrm{keV}$ with a polarization level of $\sim 99\ \%$. For all the tests performed we set the energy to $278\ \mathrm{keV}$.

The prototype detectors were firstly evaluated individually and proved to have a good performance for polarimetric measurements. Regarding the 2 layers Compton configuration: we evaluate the modulation factor *Q* and its dependence with the distance between detectors; and its potential to determine the polarization angle orientation by performing measurements at different polarization direction angles. The results showed that the modulation factor *Q* decreases for higher distances between detectors. The reason for this result is the lower scattering angles accepted for higher distances that affect the modulation factor *Q*. Regarding the potential to determine the polarization angle orientation the polarization angular resolution obtained was better that $8°$.

In order to validate our simulation and prototype design for a high-energy space telescope, the prototype must be tested and its performance analyzed in a wider energy band, 100 keV up to 600 keV. During the time slots provided to this experiment, it was not possible because the beamline ID15A had flux limitations for higher energies. The level of polarization is another parameter that we want to evaluate to determine the sensitivity of this configuration to it. The system is also being improved to allow a fine tuning of distance between the two layers and the acceptance of higher scattering angles.

2 Introduction

Astronomy in the medium-energy gamma-rays band (0.1 – 100 MeV) holds a rich promise of gravitational waves joint observation or possible dark matter products detection and will address issues such as galactic positron origin or supernovae explosion process contributing to the progression of cosmology and fundamental physics. Over the last decade, the diversity and richness of the gamma-rays sky have been revealed through the joint exploitation of instruments on-board satellites such as INTEGRAL (INTErnational Gamma-Ray Astrophysics Laboratory) and Fermi Gamma-Ray Space Telescope in the soft and high energy gamma-ray domains [1, 2]. Position, spectral and temporal analyses have now been made possible, and hence, confronted to multi-wavelength data to probe the underlying physical mechanisms of the observed sources, among them: gamma-ray bursts, novae, supernovae and their remnants, pulsars and their wind nebulae, accreting binary systems and active galactic nuclei, massive stars and stellar formation regions.

Polarization of high energy sources is one of the key observational parameter to understand the emission mechanisms and geometry of a wide number of cosmic objects such as gamma-ray bursts, pulsars and others, where some degree of polarization is expected [3]–[5]. Even though this has been known for quite some time in the scientific community, no dedicated gamma-ray polarimeter have been launched into space. In the soft gamma-ray domain only a few polarimetric measurements were possible by the SPI (Spectrometer On INTEGRAL) and IBIS (Imager on Board the INTEGRAL Satellite) instruments on-board the INTEGRAL mission [6], [7], on the Crab Pulsar, on the galactic black-hole Cygnus X-1, and on several gamma ray bursts (GRBs) [8]–[14].

CdTe based polarimeters for future high energy mission are being studied by our groups for more than a decade [15]–[23]. A series of experiments were performed at the ESRF under a ~99% polarized gamma-rays beam (MI-592/854/905/966/1074). These experiments have allowed us to assess the use of such devices to perform high sensitivity polarimetric measurements together with spectroscopy, imaging and timing in the 0.1–1 MeV energy range. The polarimetric performance was analyzed for different detector pixel sizes and thicknesses, for Laue lens focalized beams as well as for different off-axis beam inclinations, energy ranges, beam polarization angles and polarization levels. The objective is to implement this kind of detectors in a new generation of high-energy telescope mission concepts based on highly segmented multi-layer instruments and broad band Laue focusing techniques, that can achieve a sensitivity up 100 times better than current instruments. The results obtained have already motivated several partnership proposals submitted in the ESA (European Space Agency): GRI (Gamma-Ray Imager)[24], DUAL[25], ASTROGAM [26] and e-ASTROGRAM [27].

This experiment aims to bring this study to another level, closer to realistic focal plane configurations and operation modes, by developing and testing a new detector prototype configuration consisting in a 2 layer Compton spectro-imager based on 2 CdTe pixelized sensors, operated as a Compton scattering polarimeter. This new prototype configuration allows to study and to assess not only the multi-layer focal plane solution but also the scattering polarimetric performances of a 3D spectro-imager by varying the distance between the two CdTe pixel detection layers over the 100–700 keV energy range. These results will be of fundamental importance for both high efficiency Laue lens telescope focal planes and all-sky advanced Compton telescope designs for the next generation of space missions. Both solutions require the implementation of highly segmented multi-layer or 3D detection

systems with high efficiency and fine trajectory resolution to fulfil the sensitivity requirements of such future space telescope missions.

In particular, the current prototype results and conclusions will contribute to validate and boost the development of innovative concepts to address high-energy astrophysics most relevant issues within e-ASTROGAM and ASTENA (Advanced Surveyor of Transient Events and Nuclear Astrophysics) mission proposals in the framework of Work Package 9 activities of H2020 AHEAD (Integrated Activities in the High Energy Astrophysics Domain) project [28]. Within AHEAD, our group's task is to develop a configuration for e-ASTROGAM (ESA M5 call shortlisted) allowing the first space Compton and pair production polarimetric measurements. Furthermore, we will participate in development of ASTENA [29] first gamma-ray Laue lens telescope. Space polarimeters will open a new window in the high-energy Universe knowledge and Laue lens will bring the long awaited observational sensitivity leap [30].

3 Compton Scattering Polarimetry

The polarimetric performance of a high-energy detection plane is determined by the fundamental concepts associated with polarized Compton interactions and by its design. A polarized photon beam that is scattered by a detector element generates Compton scattered photons whose azimuthal distribution is not uniform. Indeed, the scattered photons' angular direction depends on its initial polarization angle. If the scattered photon goes through a new interaction inside the detector, the statistical distribution of photons angular directions defined by the two interactions (double-event) provides a modulation curve from which the degree and polarization direction of the incident beam can be derived. The azimuthal angular distribution of the scattered photons is given by the Klein-Nishina differential cross-section for linearly polarized photons:

$$\frac{d\sigma_{KN,P}}{d\Omega} = \frac{r_0^2}{2}\left(\frac{E'}{E}\right)^2\left[\frac{E'}{E} + \frac{E}{E'} - 2sin^2\theta cos^2\varphi\right] \qquad \textbf{Eq. 3.1}$$

where r_0 is the classical electron radius, E and E' are, respectively, the energies of the incoming and outgoing photons, θ the angle of the scattered photons and ϕ is the angle between the scattering plane (defined by the incoming and outgoing photon directions) and incident polarization plane (defined by the polarization direction and the direction of the incoming photon). As can be seen from Eq. 3.1, after fixing all other parameters the scattering probability varies with the azimuthal angle φ and its maximum and minimum arises for orthogonal directions. For $\varphi = 0°$ the cross-section reaches a minimum and for $\varphi = 90°$ the cross-section reaches a maximum.

The polarimetric performance of an instrument can be evaluated by calculating the polarimetric modulation factor, Q_{100}, of double-event distribution generated by a 100% polarized beam, and is defined as the amplitude of the modulation curve:

$$Q_{100} = \frac{N_{//} - N_{\perp}}{N_{//} + N_{\perp}} \qquad \textbf{Eq. 3.2}$$

where $N_{//}$*and* $N_{\perp}$, are the double-events integrated over two orthogonal directions defined over the detector plane along the maxima and minima of the modulation curve [3]. A higher value of *Q* means that the instrument responds to polarized radiation with a larger modulation and the effect of statistical fluctuations is, in proportion, lower.

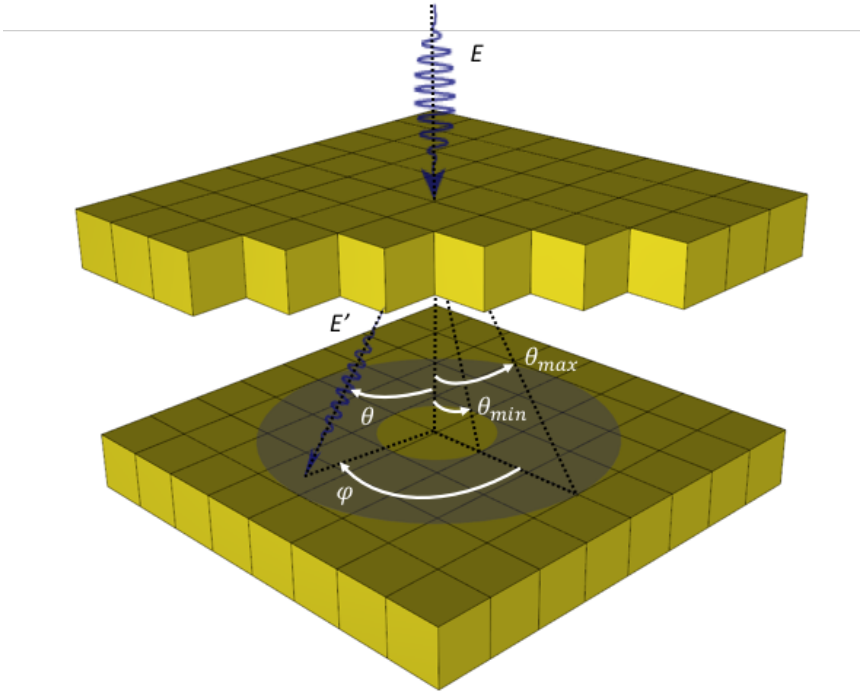

Figure 1 - Layout of a bi-planar polarimeter. Polarization of photons is measured by selecting those events which are scattered by the top detection plane and subsequently absorbed by the bottom detector. The accepted events have to be scattered in the hollow cone defined by θ_{min} and θ_{max}.

For a bi-planar polarimeter as the one schematized in Figure 1, the photons are scattered in the top detector, depositing part of their energy there, and then, are absorbed by the bottom detection. The scattering direction is defined by the hit pixels in the two detectors. In order to calculate the modulation factor, the events are selected in a hollow cone defined by θ_{min} and θ_{max} (Figure 1). An estimate of the modulation factor as function of θ_{min} and θ_{max} can be computed taking into account the geometry of the instrument and the angular dependence of the differential cross section of Compton scattering. Using equation Eq. 3.2 the modulation factor is given by:

$$Q(\varepsilon, \theta_{min}, \theta_{max}) = \frac{M(\varepsilon, \varphi = 90°, \theta_{min}, \theta_{max}) - M(\varepsilon, \varphi = 0°, \theta_{min}, \theta_{max})}{M(\varepsilon, \varphi = 90°, \theta_{min}, \theta_{max}) + M(\varepsilon, \varphi = 0°, \theta_{min}, \theta_{max})} \qquad \textbf{Eq. 3.3}$$

where ε is the energy of the incident photon in units of electron rest energy, $\varepsilon = E\ /\ (m_e\ c^2)$ and $M(\varepsilon, \varphi, \theta_{min}, \theta_{max})$ is the modulation curve integrated over the range of θ values and can be derived using Eq. 3.1 and knowing the ratio between the photon energy before and after the scattering given by the Compton physics $E' = E\ /\ (1 + \ \varepsilon\ (1 - cos\theta))$:

$$M(\varepsilon, \varphi, \theta_{min}, \theta_{max}) = \int_{\theta_{min}}^{\theta_{max}} \left(\frac{1}{1 + \varepsilon(1 - cos\ (\theta)} + \frac{1}{[1 + \varepsilon(1 - cos(\theta)]^3} - \frac{2sin^2\theta\ cos^2\varphi}{[1 + \varepsilon(1 - cos(\theta)]^2} \right) sin\theta\ d\theta \qquad \textbf{Eq. 3.4}$$

In Figure 2 we report the modulation factor as a function of θ_{min} and θ_{max} for 300 keV photons. As can be seen the value of the modulation factor increases monotonically with θ_{min} and θ_{max} and the higher value obtained is when θ_{min} and θ_{max} have values $\sim 90°$. This is the case of a thin single plane detector. For our prototype, the values of θ_{min} and θ_{max} depends on the size of the detectors and the distance between them. The latest parameter can be adjusted therefore we evaluated the modulation factor for different values of θ_{min} and θ_{max}, however θ_{min} is limited due to the low energy threshold of the top detector.

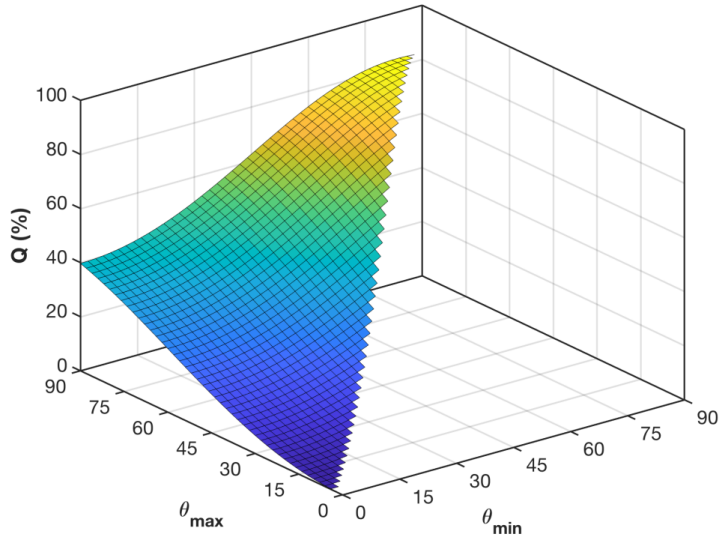

Figure 2 - Behaviour of the modulation factor as a function of θ_{min} and θ_{max}. The energy of the incident photons is 300 keV.

4 Compton-POLCA IV system main characteristics

In this chapter, it is described the system developed. It consists in the following subsystems:

- Detection System: Two detectors of 64 pixels each.
- Front-end electronics: 8, 16 channels ASICs.
- Read-out electronics (TAKES): 128 channel capability, coincidence circuitry and analog -to-digital converter (10-bit ADC).
- NI DAQ PXI-6533 – Data acquisition computer interface.
- Computer: data collecting system operating under user written software in LabView environment.

The detection system was developed for this experiment, the other sub-systems were previously used in past experiences at the ESRF: MI-854/905/966/1074 and are well described on the respective reports. Nevertheless, we summarize each subsystem here highlighting the changes from the previous experiments.

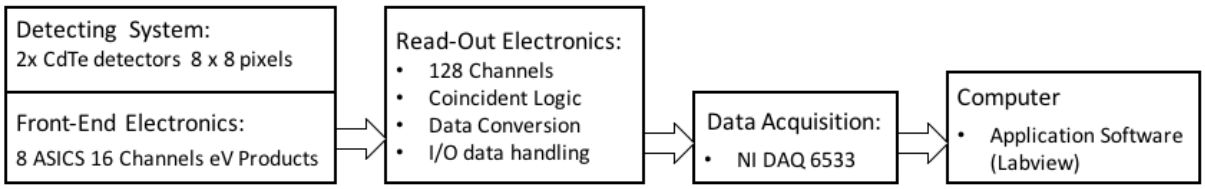

Figure 3 – Block diagram of the pixelated detectors electronic chain and DAQ system used in this work (see text for details).

4.1 Detection System

The detectors available for this work are two 8×8 pixels CdTe sensors fabricated by ACRORAD. The dimensions of each pixel are 1.9×1.9 mm with an inter-pixel gap of 0.1 mm. The detector has a solid electrode (cathode) on one side and 64 pixels (anodes) on the other side (Figure 4 left), being attached to a mount base that routes the connections to a typical pin configuration (Figure 4 right).

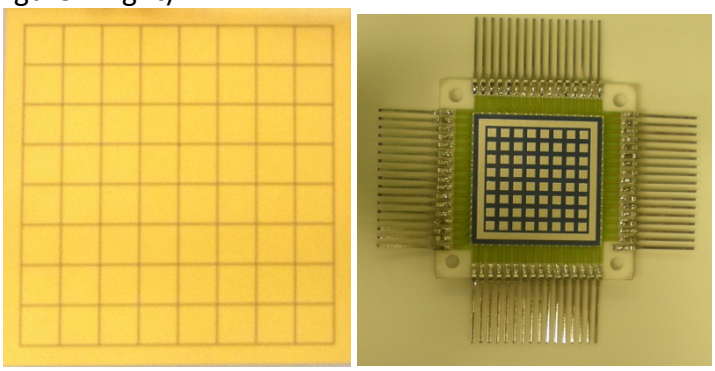

Figure 4 –The pixelated view of ACRORAD 8×8 CdTe matrix (left) with the respective bonding board (right) used in this work.

Each detector was soldered in an individual PCB. The connection between the PBCs is made through a 64 pin flat cable to allow the movement between the two planes. The bottom detector PCB makes the interface to the Front-end Electronics through 2 high density connectors of 100 pins each. Both PCBs are enclosed in one light tight and electrically shielded container. To change the distance between planes we use hexagonal aluminum spacers, which are available in many different sizes. In Figure 5 is shown the CAD drawing POLCA IV system with the Frond-end Electronics enclosure (red box) and the detectors enclosure (transparent) with the two detectors inside. It also shows a picture of the two PCBs that support the detectors.

The Front-end Electronics used in POLCA IV is the same as the previous experiments and comprises 8 ASICs (eV Products) with 16 independent channels each, resulting in a total of 128 channels allowing the readout of the two 64 pixels detectors. These devices sensitivity varies in function of the energy band selectable gain: 1.2 up to 7.2 mV/keV, with peaking-time adjustable between 0.6 and 4 μs.

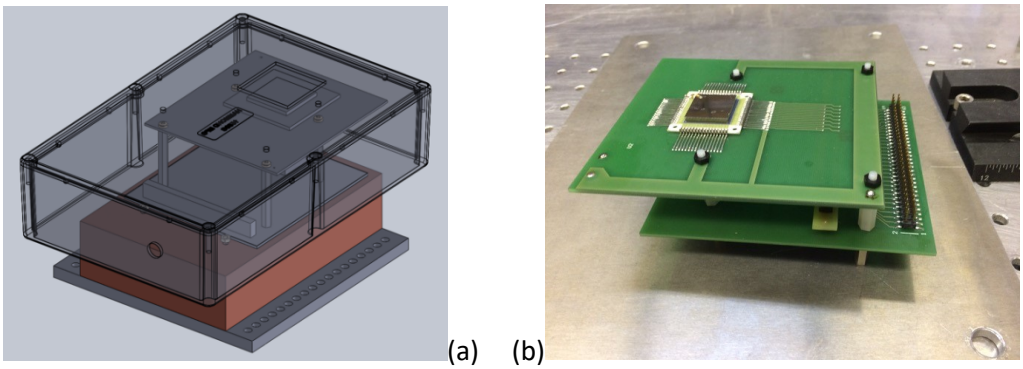

(a) (b)

Figure 5 - (a) Schematic drawing of the POLCA IV detection system. The reddish box at the bottom is the POLCA FEE. The top enclosure is transparent only to show the two pixel detectors support inside. (b) Picture of the first version of the mechanical support of the two pixels detector system. The two pixels plane are inside the same light tight and electrically shielded box.

4.2 Read-out Electronics TAKES

The signals were processed by a custom multiparametric system consisting of 128 independent channels with filters, coincidence logic and ADC (Analog-to-Digital Converter) units. When operating in coincidence mode, all signals exceeding the lower energy threshold occurring in the same coincidence time window (2 µs) are analyzed as generated by the same event. The typical irradiated pixel count rate was about 10^4 counts/s.

4.3 Data Acquisition System

This unit was based on a commercial data acquisition card PXI DAQ-6533 provided by National Instruments connected to a personal computer and controlled by a LabView application. For each event we obtained information about the number of hits, the triggered pixels and the energy deposited in each hit. The software is based in LabView and is designed for acquisition control and data analysis. The main window is presented in Figure 6. The software was mostly based on the software of the previous experiments being the main difference the addition of two pixel maps corresponding to each detector. For each TAKES channel there is a correspondence to the number of the pixel and detector.

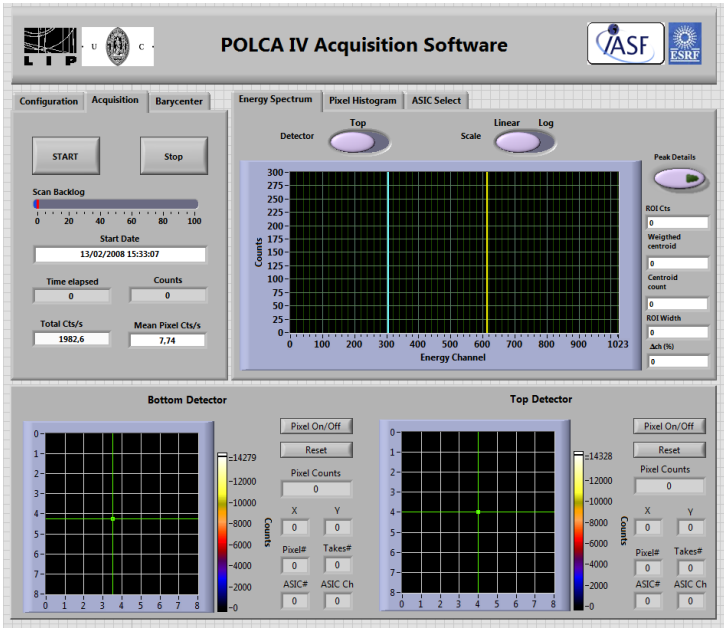

Figure 6 - Main window of the POLCA IV Acquisition Software.

5 Experiment Preparation at LIP-Coimbra

5.1 ASIC operative Setting

The ASICs used in the experiment have been used and characterized in past experiences. Each ASIC have both peaking-time and gain settable by two set of micro-switches on the ASIC board. We have to choose the operative values that are most suitable for the operation energy range that we are using at the ESRF. In [31] it was obtained the relation between the ASIC output voltage and the energy, and is given by:

$$V(\text{volt}) \cong (5.76 \times 10^3 \times E + 2.3 \times 10^{-2}) \times (G/200) \qquad \textbf{Eq. 5.1}$$

in which E is the energy in keV of the source, G is one of the 4 gain settings of the ASIC (200,100, 50 and 33 mV/fC). Using the above equation and the saturation value of the ASIC output, which is ~ 2.2 volt, we obtain the operation range of the ASIC shown in Figure 7.

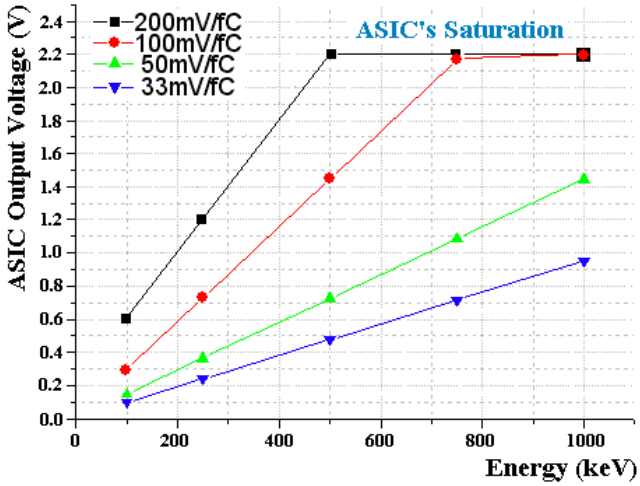

Figure 7 – The operational range of ASIC vs set gain value.

We want to use the system up to 700 keV so based on Figure 7 we set the gain to 100 mV/fC and a peaking-time of 1.2 μs. The total operation range of the system can be further adjusted using the trimmers that are available on each analog signal on the TAKES boards. To prevent the saturation of the signal in the TAKES board we interface the ASICs and the TAKES board with 12 $\text{k}\Omega$ resistors.

5.2 Detector Status before the ESRF test campaign.

In Figure 8 is shown the false color maps for both detectors obtained at LIP-Coimbra laboratory before the ESRF test campaign. This measurement was made by scanning both detectors with a uncollimated source of ^{133}Ba. Each pixel had an individual measurement with the same time and the single events of the pixel in study were then selected. To obtain the final false color that is shown we sum all the individual pixel measurements.

As can be seen the top detector is quite uniform, despite the 16 dead pixels. The bottom detector was almost unusable due to the dead pixels and the poor uniformity performance. The reason for the dead pixels is the bonding technique used to attach the detector to the support PCB. During the laboratory experiments we realize that the solders broke very easily. Fortunately, we had the opportunity to change to bottom detector during the ESRF campaign for a better and stable one. The top detector was the same for all the tests, but as will be shown in the chapter 7.1 the detector lost more pixels during all the transport and setup of the experiment.

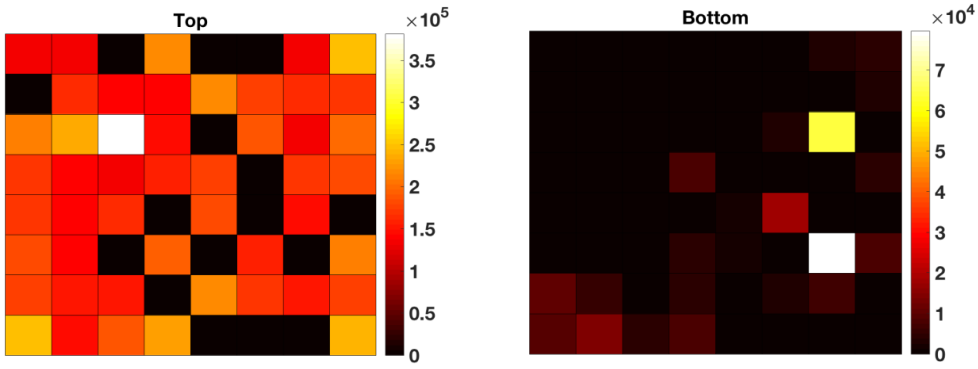

Figure 8 – False color counts maps obtained before the ESRF test campaign.

5.3 Multiparametric Electronics chain equalization

All the top detector pixel channels have been equalized at LIP-Coimbra, using an uncollimated ^{133}Ba source. The source was placed few cm above the detector cathode. To equalize the gain of each channel we used the trimmers available on each analog channel of the TAKES boards that allow a fine gain adjustment from 0.5 to 1.5 relative to the main amplifier gain.

Using as reference line the 356 keV photopeak, we have equalized the peak channels to have the centroid on channel ~ 540 using the acquisition s/w tool. During the ESRF test this detector was replaced by a new one. A summary of these results is given in Figure 9 and Figure 10 that shows the full-energy peak centroid for each pixel. The data analysis demonstrated that detector is quite uniform, with a relative standard deviation ~ 0.1%.

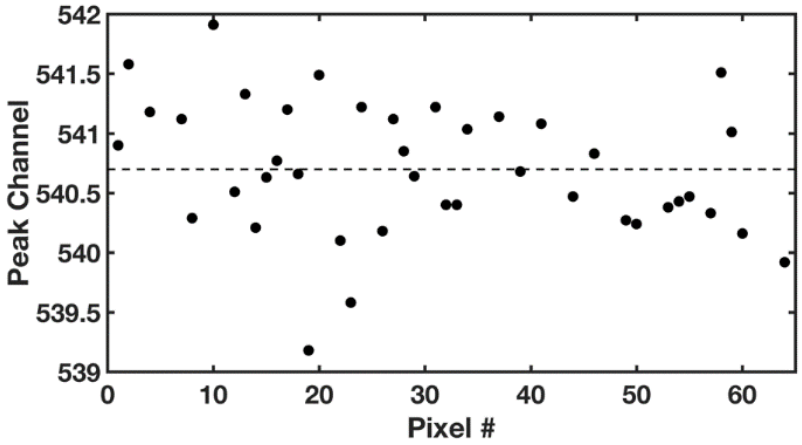

Figure 9 - Gain pixel equalization with ^{133}Ba 356 keV photopeak. The horizontal line represents the average peak channel: 540.7.

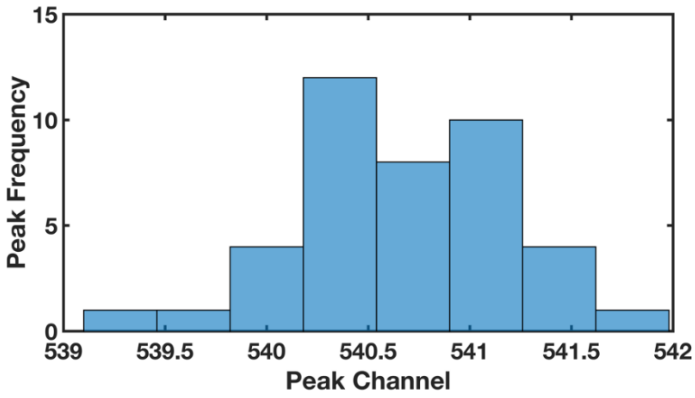

Figure 10 – Gain pixel histogram using the ^{133}Ba 356 keV photopeak.

5.4 Detector System Calibration

As second step, the detector was calibrated using radioactive sources with different gamma-rays energies in order to study the spectroscopic response and to obtain the calibration line (channel vs energy) to verify the response linearity of each pixel. During these phase, we used two uncollimated radioactive sources (Figure 11) positioned a few centimeters above the detector: ^{57}Co (122 keV) and ^{133}Ba (81 keV and 356 keV). In Figure 12 are plotted the parameters of the calibration straight line for each pixel.

In the TAKES read-out electronics, we can set the minimum energy threshold of the system. This threshold is set to prevent the low voltage electronic noise, but should be low enough to read the low energy deposited in the detector by photons in the first interaction of the Compton event. The average low energy threshold of the detection system is ~ 40 keV.

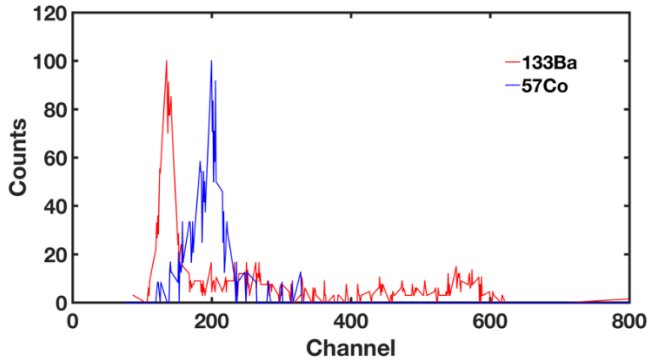

Figure 11 – Sample of a normalized spectra of the radioactive sources used to calibrate the detector in the laboratory.

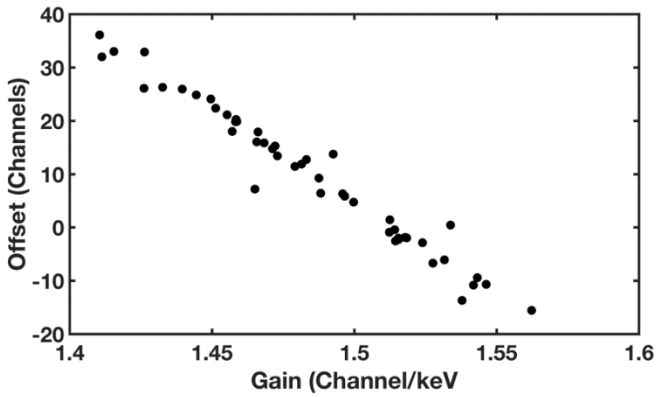

Figure 12 – The calibration parameters by a straight line fitting of the peak channel vs energy relation for each active pixel.

6 ESRF ID15 A Beamline

ID15A is dedicated to applications of high energy X-rays radiation to materials chemistry and engineering. It contains two in-line experimental hutches for high-energy X-rays experiments. The first, EH2, is for materials engineering experiments, and the second, EH3, is for materials chemistry experiments. The hutch used was the EH2 which is show on Figure 13.

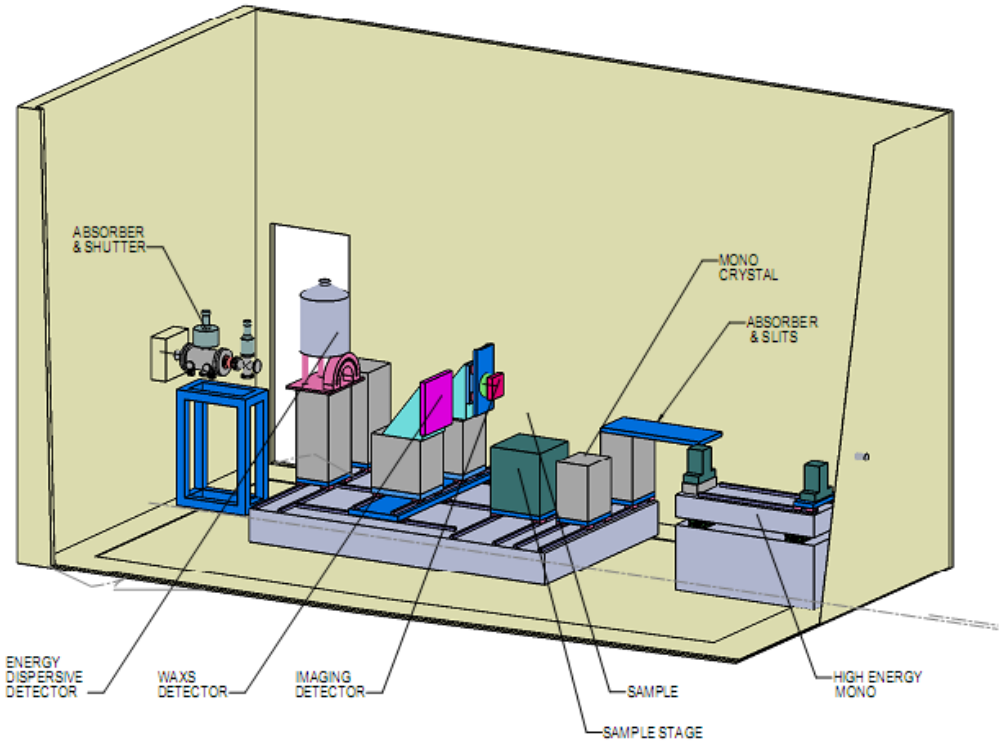

Figure 13 – General view of the hutch EH2.

ID15A has two insertion devices. One is a compact wiggler source W76, which provides a continuous spectrum up to several hundred keV gamma-rays and the second is a U22 undulator, which provides brilliant X-rays in the 30–140 keV energy range. For this experiment, the device available was the U22 undulator which delivers sufficient flux for energies up to 300 keV. For all the measurements we selected an energy of 278 keV.

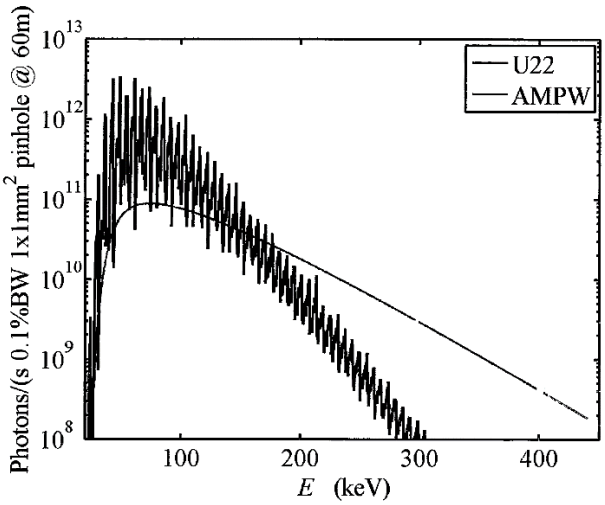

Figure 14 – Energy spectra comparison of the two insertion devices on ID15A beamline.

The detector container was mounted perpendicular to the photons beam inside a rotational stage on a XYZ positioning system as can be seen in Figure 15. All the detector subsystems (detector, power supply, multiparametric electronics) have been mounted inside the experimental hutch, leaving in the control room only the serial to parallel interface box and the computer with the NI6533 data acquisition board and the Quick-look software. Between the beam from the monochromator bench and the detector window is placed a tungsten collimator with a variable square aperture and an absorber with a triangular shape. Through the ESRF control console is possible to manage all the positioning and rotation stage, the optics hutch shutter and the absorber positioning.

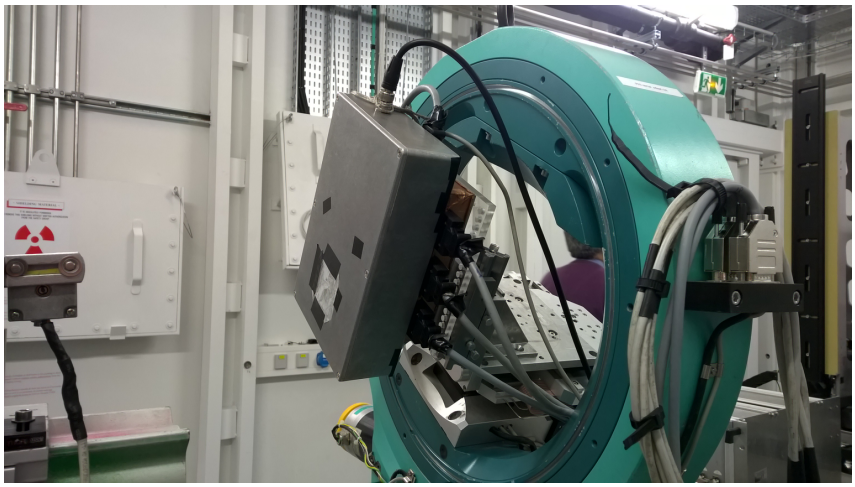

Figure 15 - The detection system mounted on the rotational stage on the XYZ micrometric positioning stages.

The experiment was divided on the following steps:

1. Pixel scan of the top detector.
2. The size of the beam was changed and aligned with the center of one of the pixels of the top plane.
3. Bottom detector was placed at 6 mm from the top one and a new pixel scan was performed with both detectors placed.
4. We choose 4 pixels to irradiate in order to evaluate to polarimetric performance of the dual polarimeter for two distances: 6 mm and 10 mm.

5. The beam was place on the center and the detector was rotated $0°$, $20°$ and $45°$ for 6 mm distance.
6. The detector was tilted $4°$.
7. During the firsts two steps another detector was used on the bottom plane. This detector had a lot of dead pixels and a poor performance, so we changed it for the subsequent tests. Nevertheless, the data acquired during these tests was used to perform the polarimetric evaluation of the top detector, since there is no interference of the bottom detector on these tests.

7 ESRF Data Analysis

The recorded data was analyzed off-line by a Matlab® software custom tool which allows the selection of single, double and multiple events (photons undergoing at least three interactions in the detection plane). These selections of events were then used for different analysis: pixel response uniformity and polarimetric analysis, both intra layer (double events on the same detector plane) and dual layer (double events in between the two detector planes). On each analysis is presented a more detailed description of the methods used.

7.1 Pixel Response Uniformity

The pixel scan allowed us to characterize the CdTe detectors. We evaluated the distribution of the gain (the full-energy peak channel), energy resolution, and relative efficiency, across each array.

The pixel scan over all the pixels was performed using the ESRF beam at $278\ \mathrm{keV}$. Both detectors were tested at the same time. In order to compensate any misalignment in between the two detectors each pixel was divided in 16 subpixels that were scanned with a $0.5 \times 0.5\ \mathrm{mm}^2$ beam for $10\ \mathrm{s}$, resulting in a total of 1024 steps (Figure 16).

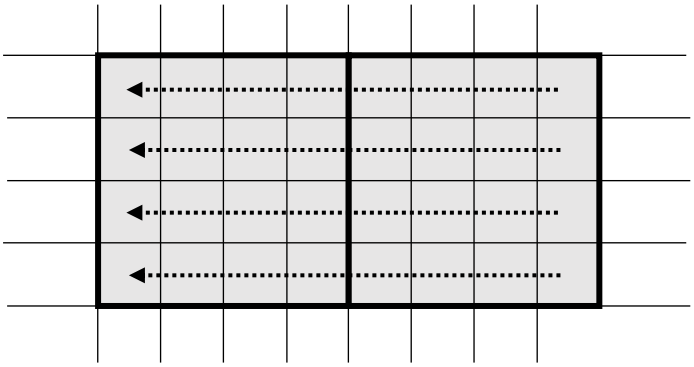

Figure 16 – Diagram of the pixel scan. The bold line corresponds to the pixels limits.

7.1.1 Detectors evaluation

Since there are dead pixels on both detectors, the pixel scan allowed to find the dead pixels and the better detector zones for the polarimetric measurements. In Figure 17 is shown the pixel maps for both detectors achieved with the pixel scans. We found that a total of 49 dead pixels: 17 on the bottom detector and 32 on the top detector.

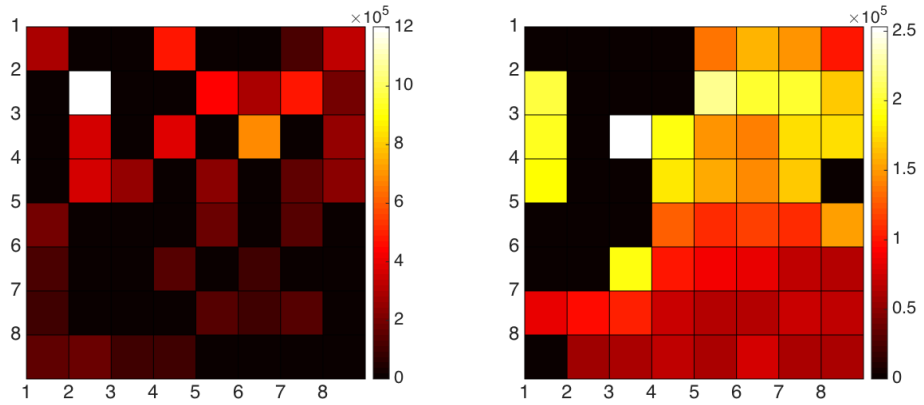

Figure 17 – Pixel maps measured during the pixel scan: left - top detector, right - bottom detector.

7.1.2 Spectroscopic performance

To evaluate the spectroscopic performance parameters we have used only the single events (i.e. events from a hit with one pixel) by fitting the corresponding full-energy peak in the spectra. A summary of these results is given in Figure 19 that shows the full-energy peak centroid and the energy resolution (FWHM) calculated for each pixel of each detector.

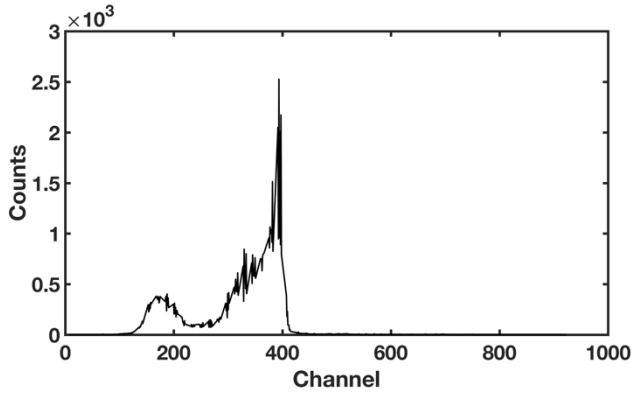

Figure 18 – A sample of energy spectrum, for 278 KeV photons beam, measured with one pixel.

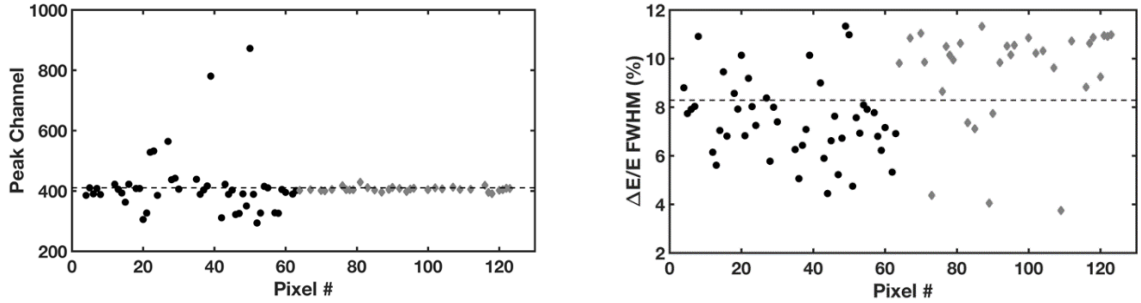

Figure 19 – The uniformity of pixel gain (full-energy peak centroid) and energy resolution of the two CdTe arrays. The different symbols refer to different detector arrays: black markers – bottom array; grey markers – top array. The horizontal lines represent the average: peak channel = 410.1; energy resolution = 8.3%.

The data analysis demonstrated that the top detector is quite uniform, with a standard deviation ~ 1.8%, while the bottom detector exhibits a gain dispersion up to 25%. The reason for this is that the top detector was previous equalized in the laboratory before ESRF campaign, but the bottom was only tested during the campaign and there was no opportunity to equalize it. This information will be useful to select the Compton events by their energy in the polarimetric analysis.

The results of the spectroscopic performances show that the bottom has a slightly better energy resolution with an average value ~ 7.5% while the top detector shows an average value ~ 9.4%. The relative standard deviation is around 21% for both detectors.

7.1.3 Event efficiency

The second step was the analysis of the efficiency uniformity with respect to the single events and double events, i.e. Compton scattered events that trigger two separate pixels inside the coincidence window. Figure 20 and Figure 21 summarizes the evaluation of the pixel relative efficiency for single and double events in the two CdTe arrays, while Table 1 reports the average values. The relative efficiency is defined as the ratio between the number of detected single or double events in the beam incidence pixel and the total detected events in the array during the same measurement.

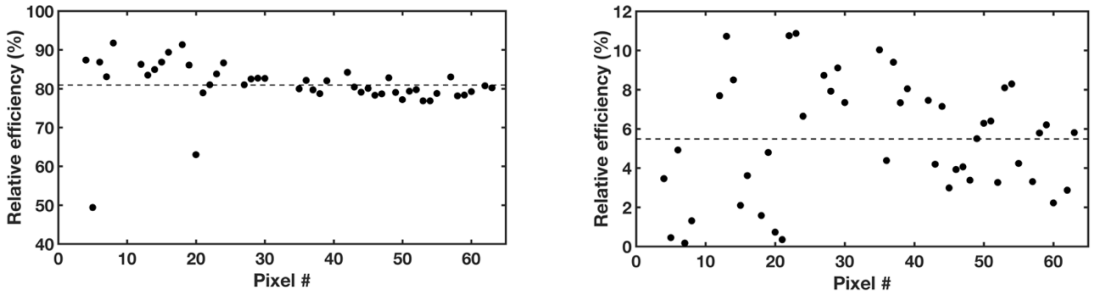

Figure 20 – Relative efficiency distribution for the tested bottom detector: single events on left and double events on right.

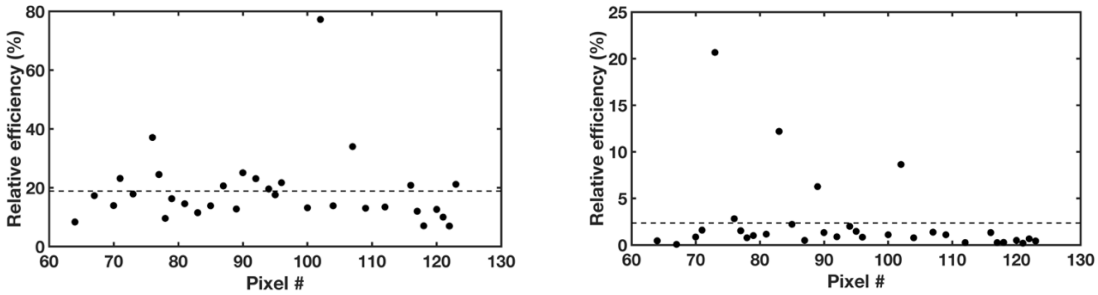

Figure 21 - Relative efficiency distribution for the tested top detector: single events on left and double events on right.

Table 1 – Relative mean efficiency of the tested CdTe arrays.

Detector	Single efficiency (%)	Double efficiency (%)
Top	18.8 ± 12.7	2.3 ± 4.2
Bottom	80.9 ± 6.6	5.5 ± 3.0

7.2 Polarimetric Performance Evaluation

7.2.1 Data Selection and Corrections

There are several effects that under certain conditions might introduce significant errors in the modulation factor *Q* measurement. However, for CdTe pixelized matrices the dominant source of error is the non-uniformity in pixel response due to material imperfections throughout the matrix crystal. It may vary by more than 25% for a significant fraction of the

pixels. Another important source of systematic errors is related to our experiment, in particular the alignment accuracy of the beam with respect to the irradiated pixel center and the alignment between detectors. In order to minimize these sources of error before each measurement we performed a complete scan of all detector pixels. The scan was performed with ESRF polarized beam at $278\,\mathrm{keV}$ for both detectors at the same time and at the laboratory with an uncollimated source. The matrix data of each detector obtained from the single events recorded in each pixel was then used to correct the inherent non-uniformities in the response of the detector pixels. We estimate the true double event counts for each pixel by:

$$N_{true} = \frac{N_{pol}}{N_{non}} N_{max} \qquad \textbf{Eq. 7.1}$$

where N_{pol} is the number of double events detected (that depend on the beam polarization level), N_{non} is the number of single events of the response map obtained when the pixel is directly irradiated and N_{max} is the maximum value among all the matrix pixels single events. By applying this method to the pixels surrounding the irradiated pixel, the error introduced by the non-uniformity of the detector matrix response is minimized thereby improving the accuracy of the calculated modulation factor *Q* .

To evaluate the polarimetric performance we selected the double events in each measurement. We separate them in intra layer interactions (double events in the same plane) and dual layer interactions (double events in the two detectors). Multiple events do not enter into our calculations since we cannot determine the order of each hit. For double events, we know which is the first interaction because this is coincident with the position of the pixel irradiated by the collimated beam and therefore during the analysis we exclude double events that do not have at least one interaction in the target pixel, e.g. chance coincidence events due to noise and flaring pixels and/or triple events in which the first interaction in the target pixel was under the low energy threshold. Because of the impinging beam was monochromatic we also applied a further simple selection of double events using the energy deposited in each hit. Knowing the beam energy, we have selected as good double events only those in which the sum of the two interactions is within a window centered at the selected beam energy. Furthermore, taking into account the Compton kinematics and the detector geometry we also evaluate the energy of each hit. Since the impinging beam has an energy of $278\,\mathrm{keV}$ for the intra layer interaction the Compton scattering angle is around $\sim 90^\circ$ we expect that the first hit has an energy $\sim 100\,\mathrm{keV}$ and the second $\sim 180\,\mathrm{keV}$. For the double layer interactions, the energy of the events depends on the scattering angles we are looking for, so we select an energy range accordingly. Lastly, due to the low energy threshold of the system, $\sim 40\,\mathrm{keV}$, we expected that the minimum scattering angle is $\sim 25^\circ$, so we exclude double events with scattering angles below this threshold.

In order to optimize the double-event histogram readout, we applied the radial bin technique (RBT) [3], by dividing the matrix into 24 radial bins of 15° each. Pixels partially crossed by angular bin lines contribute only with a fraction of the number of events equal to the fraction of its area that is in the sector - this is an approximation since real hits inside each pixel are not uniformly distributed but have a radial dependence relative to the position of the first Compton interaction of a double-event. The modulation curve, $N(\varphi)$, giving the number of double-events as a function of the azimuthal angle φ, was then obtained. The

polarimetric modulation factor *Q* was calculated from Eq. 3.2 and the polarization direction was obtained from the angle that maximizes the modulation curve.

The described data correction and analysis techniques were implemented in a MatLab based code that processed the prototype output data.

7.2.2 Intra layer polarimetric performance

The detectors used have never been tested for polarimetric measurements, only for spectral measurements in the laboratory. These tests have the aim to evaluate the polarimetric performance of each of the detector planes. In particular the result of these test type is the determination of the modulation factor *Q* of both detectors.

The first evaluation was the top detector. During this evaluation, we also made beam size tests with the top detector. We irradiate the top detector on pixel #14 and made three measurements with three different beam sizes: $0.1 \times 0.1\ \mathrm{mm}^2$, $0.5 \times 0.5\ \mathrm{mm}^2$ and $1.9 \times 1.9\ \mathrm{mm}^2$. The results are shown in Figure 22. The results show a decrease of the modulation factor *Q* with the increase of the beam size. These results are in accordance with the values obtained in previous experiments for CdTe detectors [15]–[23].

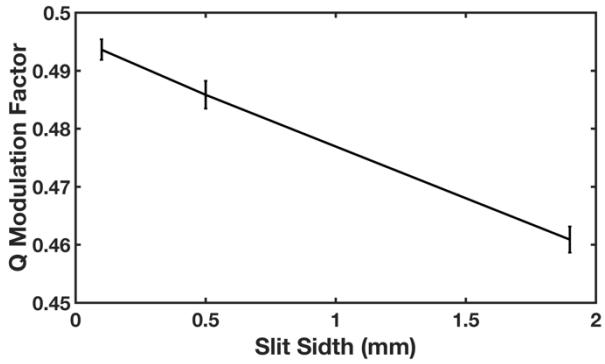

Figure 22 - Modulation factor for top plane interactions versus slit width.

The modulation factor *Q* was then evaluated for the bottom detector. In this case the detector was irradiated in pixel #62, where we were able to obtain double distributions throughout the crystal volume until second order pixels. We also rotated the detector to evaluate its potential to determine the polarization angle orientation. For these measurements the beam size was $1.0 \times 1.0\ \mathrm{mm}^2$.

Figure 23 shows false color maps resulting from double event distributions generated by a $278\ \mathrm{keV}$ monochromatic beam with polarization angles at 0° and 20°. As can be seen the double events are not uniformly distributed around the irradiated pixel for a polarization angle of 0°. As expected from theory, a maximum number of Compton photons were detected in the pixels along the direction defined by top-center-bottom of the matrix. Inside the experimental hutch it corresponds to the vertical direction. This matches with the fact that the beam polarization is horizontal inside the hutch since the polarization is always perpendicular to the maximum intensity direction. When the detector matrix is rotated by 20° the projection of the polarization in the detector plane is also rotated by the same amount.

Table 2 - Measured polarization angle and modulation factor. Bottom plane interactions.

Polarization Angle (°)	Measured Angle (°)		Modulation Factor *Q*
0	10.1	(2.1 , 18.1)	0.369 ± 0.003
20	24.1	(17.4 , 30.7)	0.349± 0.007

From the false color pixel maps obtained we estimated the modulation of the double events distribution recorded inside a 15° radial bin centered on the CZT pixel matrix. The resulted modulation was fitted with a sinusoidal function that allow the observed polarization angle to be determined. Figure 23 illustrates the modulation (fitted sinusoid represented just for guideline purposes) obtained when the beam polarization is oriented through 0° and 20°. **Erro! A origem da referência não foi encontrada.** shows the measured polarization angle as a function of the effective ESRF beam polarization angle. Overall analysis of these results shows a good agreement between measured polarization angle and the effective beam polarization angle.

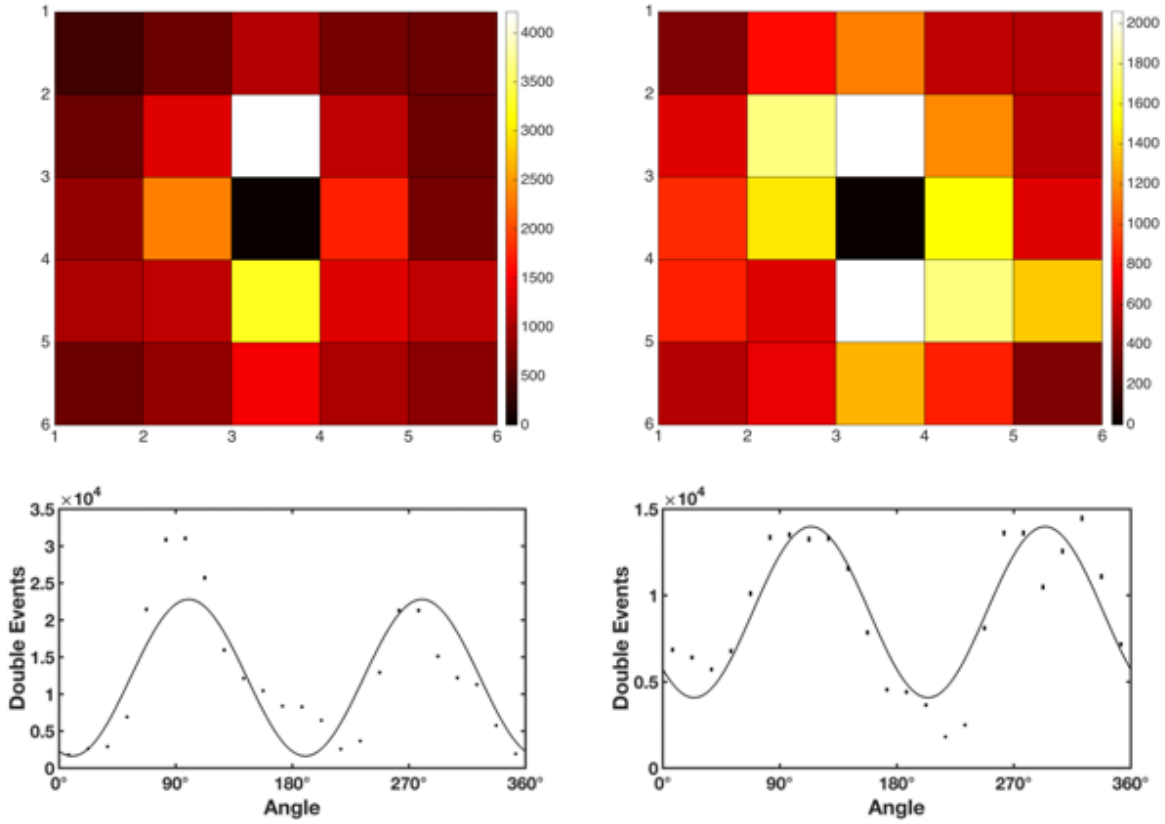

Figure 23 - Distributions and false color pixel maps for polarization angles of 0°and 20°. Bottom plane interactions.

7.2.3 Dual layer polarimetric performance

These tests have the aim to evaluate the polarimetric performance of a dual plane polarimeter. We are searching for the double events that firstly interact in the top plane by Compton process and then the scattered photon hit the bottom detector.

We made three tests: polarimetric evaluation of four corner pixels for two distances between planes; polarimetric evaluation for three polarization direction angles; polarimetric evaluation for one tilt rotation. For these measurements, the beam size was 1.0×1.0 mm^2.

Modulation factor *Q* vs distance

The aim of these experiment was to evaluate the modulation factor Q in function of the distance between detectors. These tests were done pointing the collimated beam onto four corner pixels on the top detector and we selected the double events that interacted in the two planes. By irradiating the matrix corner pixels we are able to obtain double event distributions throughout the crystal volume until fourth order pixels for two distances between detectors: $6\ \mathrm{mm}$ and $10\ \mathrm{mm}$. These corresponds to scattering angles between $\theta_{min}{\sim}10°$ to $\theta_{max}{\sim}66°$ for $6\ \mathrm{mm}$ distance and $\theta_{min}{\sim}6°$ to $\theta_{max}{\sim}42°$ for $10\ \mathrm{mm}$ distance. Due to the low energy threshold of the system $\sim 40\ \mathrm{keV}$ we expected that the minimum scattering angle is $\sim 25°$ so we just used the double events of pixels that are above this threshold. In Table 3 in shown the modulation factor Q for the four pixels studied. In Figure 24 is shown the average modulation factor Q of the four pixels for the two distances and the standard deviation.

Table 3 – Modulation factor *Q* for 6 mm and 10 mm distances between planes. The $\theta_{min}{\sim}25°$ for both distances.

Distance		6 mm	10 mm
θ_{max}		$66°$	$42°$
		Modulation factor *Q*	
Pixel #	15	0.124 ± 0.012	0.071 ± 0.010
	22	0.143 ± 0.007	0.063 ± 0.008
	55	0.146± 0.016	0.097 ± 0.023
	59	0.099 ± 0.005	0.064 ± 0.012

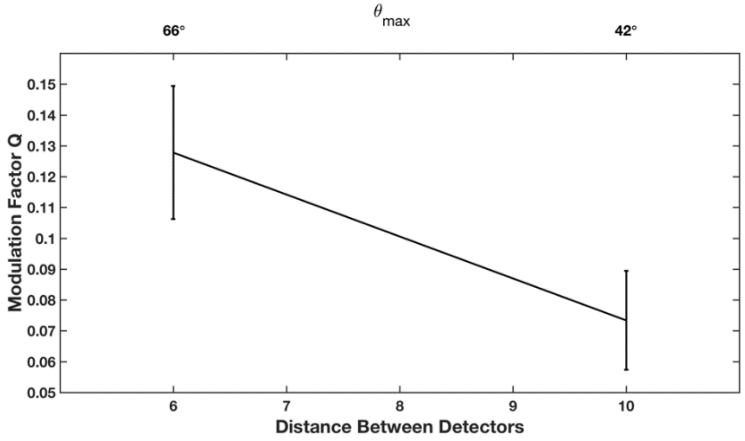

Figure 24 - Average modulation factor Q of the four pixels for the two distances and the standard deviation.

The results show a decrease of the factor *Q* when the distance between planes increased as expected. As shown previous in section 3 the modulation factor increases monotonically with θ_{min} and θ_{max}. For both cases $\theta_{min}{\sim}25°$, therefore increasing the distance will decrease the θ_{max} and the modulation factor *Q* will follow this tendency.

Polarization direction

The aim of these tests is to evaluate the dual plane detector potential to determine the polarization angle orientation. These tests were done pointing the collimated beam onto a central pixel. After each data acquisition the detector was rotated to 20°, and 45°. For these measurements, the beam size was 1.0×1.0 mm^2.

From the maps we estimated the modulation of the double events distribution recorded inside a 15° radial bin centered on the CZT pixelized matrix. The resulted modulation was fitted with a sinusoidal function that allow the observed polarization angle to be determined. Figure 25 illustrates the modulation (fitted sinusoid represented just for guideline purposes) obtained when the beam polarization is oriented through 0°, 20°, and 45°.

Table 4 shows the measured polarization angle as a function of the effective ESRF beam polarization angle. Overall analysis of these results shows a good agreement between measured polarization angle and the effective beam polarization angle. The error of most of the measured polarization angles lie within a few degrees.

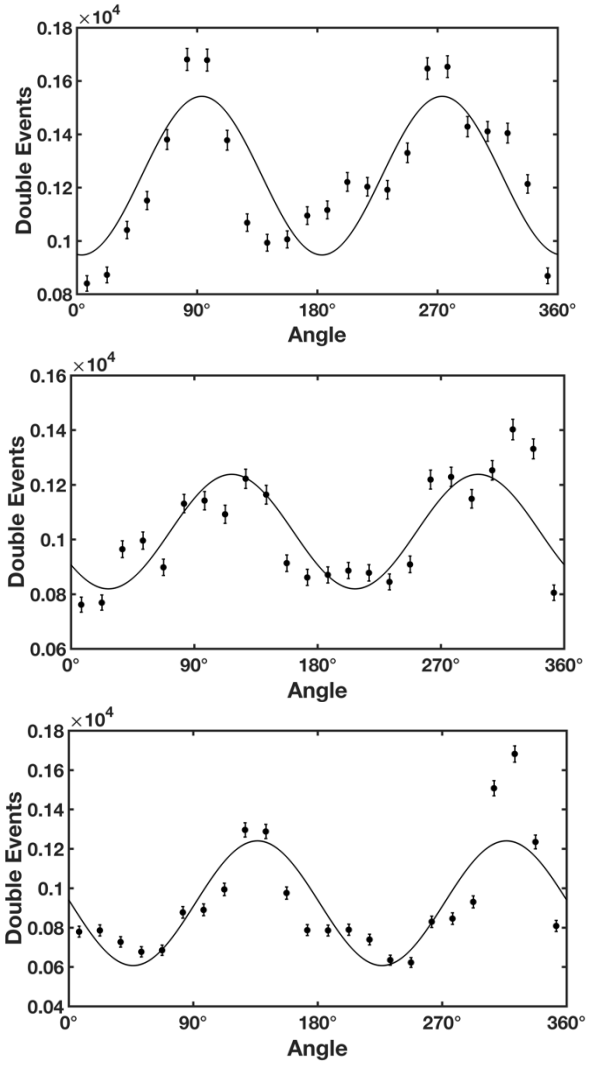

Figure 25 - Distributions for polarization angles of 0°, 20° and 45°. Top to bottom plane interactions.

Table 4 – Measured polarization angle and modulation factor. Top to bottom plane interactions.

Polarization Angle (°)	Measured Angle (°)		Modulation Factor *Q*
0	3.5	(-5.1 , 12.1)	0.20 ± 0.01
20	27.3	(17.5 , 37.1)	0.17 ± 0.02
45	46.5	(37.5 , 55.5)	0.15 ± 0.01

Tilt Rotations

The last test was to evaluate the modulation factor Q when the detector is tilted 4°. The distance between detectors was 10 mm and the beam size is 1.0×1.0 mm^2.The tilt rotation causes misalignment in the beam and the detectors. Because we were interested in the top to bottom interactions we centered the beam in a bottom detector pixel so we cannot produce asymmetries in the bottom detector modulation, as the upper detector is used only as a scattering detector so the beam position does not matter, we just need to know which top pixel the first interactions occurs.

The results are shown in Table 5 and shows the decrease on *Q* when the detector is tilted as expected. This study shows once more the importance of a pointing system with accuracy better than 1° for an instrument designed for polarimetry. This accuracy should be sufficient so that double event distributions can be read directly with no further need of correction methods.

Table 5 - Measured polarization angle and modulation factor. Top to bottom plane interactions.

Tilt Angle (°)	Measured Angle		Modulation Factor Q
0	3,5	(-5.1 , 12.1)	0.20 ± 0.01
4	9,92	(-18.5 , 38.3)	0.17 ± 0.01

8 Conclusions and Further Work

This was the first time that a bi-planar configuration detector was test as a polarimeter. The results showed that a future polarimeter with multi-layer configuration is potentially suited to perform polarimetric measurements for high energy astrophysics.

The detectors used were firstly evaluated individually and proved to have a good performance for polarimetric measurements. Regarding the 2 layers Compton configuration: we evaluate the modulation factor *Q* and its dependence with the distance between layers as well as its potential to determine the polarization angle orientation by performing measurements at different polarization direction angles. The results showed that the modulation factor *Q* decreases for higher distances between detectors. The reason for this result is the lower scattering angles for higher distances that affect the modulation factor *Q*. Regarding the potential to determine the polarization angle orientation the polarization angular resolution obtained was better that $8°$.

A new polarimetric experiment with a multi-layer prototype is being prepared. A new prototype electromechanical design is being implemented that will allow to study the polarimetric performances in a wider energy range and to analyze in a finer pace *Q* vs distance between layers. The requirements for a future experiment are described below:

- In spite the good performance during the experiment, the detector bonds were mechanically weak and broke very easily, this constrained unexpectedly the experiment. In the next experiment we will use bare detectors with the same characteristics with a new electronic arrangement;
- The time consuming and sensitive method to change distances between planes was another constrain that limited the experiment to two distances. The new configuration incorporates a micrometric system that can adjust the distance between detectors outside the detectors enclosure. We are also planning to use a new flexibly high-density cable to connect the top plane to the ASICs, with enough length to match the distances we intend to study;
- Different energy thresholds for the top and bottom detector. This could be achieved be separating the ASICs for each detector, i.e., an ASIC must not be shared in both detectors. In this configuration, the gain of each detector can be adjusted in the ASIC micro switches available. We can set the top detector for low energy photons and the bottom for high energy photons, so we can reduce the scattering angle of the photons that are scattered in the top detector;
- A DC-DC bias circuit implemented outside the detector box to avoid noise and heat sources near the detector planes;
- Improve x-y alignment between planes. This will be achieved by a new micrometric system that allow the movement of the top plane relatively to the bottom one. If the movement range in one direction is long enough we can also test the prototype for higher scattering angles;
- Concerning the available beam at the ESRF, we were only able to test the setup for one energy because of the time-consuming method of changing energies at the ID 15A beamline. Furthermore, the energy tested was not the most convenient for our detectors due to Compton kinematics. For better results, we need to increase the beam energy so the first interaction could have sufficient energy to be detected and produce lower scattering angle photons. Ideally, for further measurements, we would prefer to use the wiggler source W76 on ID15A beamline that was not available in 2017 and provides a continuous spectrum up to 700 keV or more.

For these reasons, it is of major importance to perform a new campaign at the ESRF. We plan to test a new version of the multi-layer prototype system that allow to analyze the modulation factor *Q* as function of the distance between layers with a fine pace, in a wider energy band, allowing to simulate realistic polarimetric performances of multi-layer and 3D detector solutions in space configuration conditions. 3D detectors are the most promising focal plane solutions for hard X- and soft γ-ray missions, since they will address the following requirements: high scattering efficiency, achievable with increased thickness; high modulation factor achievable with better position sensitive detection; fine spectroscopy allowing effective background rejection and good event selection. The current prototype results and conclusions are determinant to validate and boost the development of innovative

concepts to address high-energy astrophysics most relevant issues within e-ASTROGAM and ASTENA missions in the framework of H2020 AHEAD project.

References

[1] N. A. Gehrels and C. Winkler, "International Gamma-Ray Astrophysics Laboratory (INTEGRAL): A future ESA mission for gamma-ray astronomy," in *Proc. SPIE 2806, Gamma-Ray and Cosmic-Ray Detectors, Techniques, and Missions*, 1996, p. 210.

[2] A. A. Moiseev, "Gamma-ray Large Area Space Telescope: Mission overview," *Nucl. Instruments Methods Phys. Res. A*, vol. 588, no. 1–2, pp. 41–47, Apr. 2008.

[3] F. Lei, A. J. Dean, and G. L. Hills, "Compton Polarimetry in Gamma-Ray Astronomy," *Space Sci. Rev.*, vol. 82, no. 3, pp. 309–388, 1997.

[4] R. Bellazzini and F. Muleri, "X-ray polarimetry: A new window on the high energy sky," *Nucl. Instruments Methods Phys. Res. A ,* vol. 623, no. 2, pp. 766–770, 2010.

[5] M. McConnell, "X-Ray and Gamma-Ray Polarimetry," *Astro2010 Astron. Astrophys. Decad. Surv. Sci. White Pap. no. 198*, 2009.

[6] C. Winkler and T. J.-L. Courvoisier, "The INTEGRAL mission," *Astron. Astrophys.*, vol. 411, no. 1, pp. L1–L6, 2003.

[7] P. Ubertini, "IBIS : The Imager on-board INTEGRAL," vol. 139, 2003.

[8] A. J. Dean, et al., "Polarized gamma-ray emission from the crab.," *Science*, vol. 321, no. 5893, pp. 1183–5, 2008.

[9] M. Forot, "Polarization of the Crab pulsar and nebula as observed by the Integral/IBIS telescope," p. 15, 2008.

[10] D. Götz, "Variable polarization measured in the prompt emission of GRB 041219A using IBIS on board INTEGRAL," no. 100, p. 7, 2009.

[11] P. Laurent, et al., "Polarized Gamma-Ray Emission Cygnus X-1," vol. 332, no. April, pp. 438–440, 2011.

[12] D. Götz, "The polarized gamma-ray burst GRB 061122," *Mon. Not. R. Astron. Soc.*, vol. 431, no. 4, pp. 3550–3556, 2013.

[13] D. Götz, "GRB 140206A: the most distant polarized Gamma-Ray Burst," vol. 8, no. August, pp. 1–8, 2014.

[14] P. Moran, "Multi-wavelength and Polarisation Studies of Pulsars: the Crab, Vela, and PSR J0205+6449," National University of Ireland, Galway, 2014.

[15] E. Caroli and J. B. Stephen, "A CdTe position sensitive spectrometer for hard X- and soft gamma-ray polarimetry," *Nucl. Instruments Methods Phys. Res. A*, vol. 477, no. 1–3, pp. 567–573, 2002.

[16] E. Caroli and N. Auricchio, "A study of prototype CdTe hard X- and gamma-ray detectors," *Nucl. Instruments Methods Phys. Res. A*, vol. 513, no. 1–2 SPEC. ISS., pp. 350–356, 2003.

[17] R. M. Curado Da Silva, N. Auricchio, and E. Caroli, "Hard X- And Soft Gamma-ray Polarimetry with CdTe Array Prototypes," *IEEE Trans. Nucl. Sci.*, vol. 51, no. 5, pp. 2478–2484, 2004.

[18] R. M. Curado Da Silva, E. Caroli, et al., "Polarimetric performance of a Laue lens gamma-ray CdZnTe focal plane prototype," *J. Appl. Phys.*, vol. 104, no. 8, pp. 1–7, 2008.

[19] E. Caroli, R. M. Curado Da Silva, et al., "A polarimetric experiment with a laue lens and CZT pixel detector," *IEEE Trans. Nucl. Sci.*, vol. 56, no. 4, pp. 1848–1854, 2009.

[20] S. Antier, et al., "Fine pitch CdTe-based Hard-X-ray polarimeter performance for space science in the 70-300 keV energy range," *Nucl. Inst. Methods Phys. Res. A*, vol. 787, pp. 297–301, 2011.

[21] R. M. Curado Da Silva, et al., "Polarimetry study with a CdZnTe focal plane detector," *IEEE Trans. Nucl. Sci.*, vol. 58, no. 4 PART 2, pp. 2118–2123, 2011.

[22] R. M. Curado Da Silva, E. Caroli, et al., "Polarization degree and direction angle effects on a CdZnTe focal plane performance," *IEEE Trans. Nucl. Sci.*, vol. 59, no. 4 PART 3, pp. 1628–1635,

2012.
[23] M. Pinto, R.M. Curado da Silva, et al., “Polarimetric analysis of a CdZnTe spectro-imager under multi-pixel irradiation conditions,” *Nucl. Instruments Methods Phys. Res. A*, vol. 840, pp. 69–76, 2016.
[24] J. Knödlseder et al., “GRI: focusing on the evolving violent Universe,” 2007.
[25] P. von Ballmoos, “A DUAL mission for nuclear astrophysics,” *Exp. Astron.*, vol. 34, no. 2, pp. 583–622, 2012.
[26] M. Tavani, “ASTROGRAM - Summary of a proposal submitted for the ESA M4 Mission Programme,” 2015.
[27] M. Hernanz, “The e-ASTROGAM mission,” no. 2, pp. 10–12, 2016.
[28] “AHEAD (Integrated Activities in the High Energy Astrophysics Domain) project ref. 654215.” [Online]. Available: http://ahead.iaps.inaf.it/. [Accessed: 23-Feb-2018].
[29] Virgilli and C. da Silva, “The Advanced Surveyor of Transient Events and Nuclear Astrophysics (ASTENA) mission within AHEAD project,” 2018.
[30] A. De Angelis, et al., “The e-ASTROGAM mission (exploring the extreme Universe with gamma rays in the MeV-GeV range),” Nov. 2016.
[31] E. Caroli, et al., “POLCA II (POLarimetry with CZT Arrays) USER MANUAL for ESRF 2007 tests,” 2008.